mater.scichina.com link.springer.com

Published online 6 September 2021 | https://doi.org/10.1007/s40843-021-1758-5
Sci China Mater 2022, 65(2): 413–421

Controlling metallic Co^0 in ZIF-67-derived N-C/Co composite catalysts for efficient photocatalytic CO_2 reduction

Fei-Fei Chen[†], Jianfeng Chen[†], Ya-Nan Feng, Lingyun Li[*] and Yan Yu[*]

ABSTRACT **An efficient photocatalytic CO_2 reduction has been reported in ZIF-67-derived-Co nanoparticles (NPs) encapsulated in nitrogen-doped carbon layers (N-C/Co). This work demonstrates that the pyrolysis temperature is crucial in tuning the grain size and components of metallic Co^0 of N-C/Co composite catalysts, which optimizes their photocatalytic activities. Syntheses were conducted at 600, 700, and 800°C giving the N-C/Co-600, N-C/Co-700, and N-C/Co-800 samples, respectively. N-C layers can well wrap the Co NPs obtained at a low pyrolysis temperature (600°C) owing to their smaller grains than those of other samples. A high metallic Co^0 content in the N-C/Co-600 sample can be attributed to the effective inhibition of surface oxidation. By contrast, the surface CoO_x oxides in the N-C/Co-700 and N-C/Co-800 samples cover inside Co cores, inhibiting charge separation and transfer. As a result, the N-C/Co-600 sample yields the best photocatalytic activity. The carbon monoxide and hydrogen generation rates are as high as 1.62×10^4 and 2.01×10^4 μmol g^{-1} h^{-1}, respectively. Additionally, the Co NPs make composite catalysts magnetic, enabling rapid and facile recovery of catalysts with the assistance of an external magnetic field. This work is expected to provide an instructive guideline for designing metal-organic framework-derived carbon/metal composite catalysts.**

Keywords: ZIF-67, Co nanoparticles, N-doped C, photocatalysis, CO_2 reduction

INTRODUCTION

The increase in global average temperature and sea level can be attributed to the greenhouse effect caused by excessive carbon dioxide (CO_2) emissions [1]. Photocatalytic CO_2 reduction has recently drawn much attention because solar energy is a clean, sustainable, and economical energy source [2–4]. Photocatalytic CO_2 reduction is attractive because CO_2 molecules can be converted into solar fuels [5–7]. In this way, both CO_2 accumulation and energy crisis are ameliorated.

The main steps of photocatalytic CO_2 reduction include light absorption, electron-hole separation as well as transfer, and surface redox reaction [8,9]. Current research focuses on the enhancement of heterogeneous photocatalysts in the three steps [10–12]. Transition metal-based catalysts have been considered ideal photocatalysts for efficient photocatalytic CO_2 reduction owing to their high intrinsic activities and abundant sources [13–15]. Generally, the transition metal-based catalysts could strongly bind CO_2 molecules and provide sites to accept photoexcited electrons transferred from semiconductors or photosensitizers [16,17]. However, transition metal-based catalysts suffer from severe agglomeration (e.g., metal nanoparticles (NPs)) as well as unsatisfactory charge separation and transfer.

Incorporating carbon-based materials into the construction of carbon/transition metal composite catalysts can address the aforementioned challenge. Carbon-based materials with high chemical stability are wonderful supports to disperse metal species [18,19]. Additionally, carbon-based materials usually have good conductivity. Introducing conductive substances is one of the most powerful ways to promote charge transfer [20,21]. On the basis of these considerations, the combination of transition metals and carbon materials will improve photocatalytic CO_2 reduction.

Metal-organic frameworks (MOFs) are crystalline porous coordination polymers. They are constructed by metal nodes and organic ligands in a highly ordered arrangement [22,23]. Particularly, MOFs are ideal precursors for the controlled preparation of catalysts owing to their tunable components and ordered structure [24–26]. For instance, direct pyrolysis of MOFs under Ar or N_2 atmosphere produces composites of carbon materials and metals. In such a composite, metals were typically encapsulated in carbon layers [27–29]. The outer few-layer carbon can avoid severe agglomeration of metal NPs and effectively protect the metallic core from harsh environments. Besides, the synergistic effect of carbon materials and metals was expected to accelerate catalytic reactions [30,31]. These special features make MOF-derived composite catalysts ideal for photocatalytic CO_2 reduction. For example, Zhao *et al.* [32] reported cobalt-carbon composite photocatalysts with Co-MOF74 sheets as precursors. The carbon monoxide (CO) generation rate was 448 μmol g^{-1} h^{-1}. Similarly, Lin *et al.* [33] reported nickel/carbon composite photocatalysts with spherical Ni-MOFs as precursors. The CO generation rate was as high as 9000 μmol g^{-1} h^{-1}. Despite these innovative studies, the product yield from photocatalytic CO_2 reduction is unsatisfactory.

In this work, we report nitrogen-doped carbon/cobalt (N-C/Co) composite catalysts with ZIF-67 nanocubes as precursors. The grain size and components of N-C/Co composite catalysts can be tuned by controlling pyrolysis temperatures to optimize photocatalytic activities. Co NPs in a N-C/Co-600 sample obtained at a low pyrolysis temperature (600°C) are smaller than those obtained at higher temperatures, N-C/Co-700 (700°C) and

Key Laboratory of Advanced Materials Technologies, College of Materials Science and Engineering, Fuzhou University, Fuzhou 350108, China
[†] These authors contributed equally to this work.
[*] Corresponding authors (emails: lilingyun@fzu.edu.cn (Li L); yuyan@fzu.edu.cn (Yu Y))

N-C/Co-800 samples (800°C), respectively. Small Co NPs encapsulated in N-C layers inhibit surface oxidation, maintaining a high content of metallic Co^0. In addition, the N-C/Co-600 sample also contains higher pyridinic-N and pyrrolic-N contents than the N-C/Co-700 and N-C/800 samples. The photoelectrochemical characterizations confirm that the N-C/Co-600 sample exhibits the most efficient charge transfer owing to its structure and components. As a result, the N-C/Co-600 sample yields the maximum CO_2 *via* photocatalytic CO_2 reduction compared with the N-C/Co-700 and N-C/Co-800 samples.

EXPERIMENTAL SECTION

Preparation of ZIF-67 precursors

ZIF-67 nanocubes were prepared *via* a coprecipitation method [34]. Typically, an aqueous solution (20 mL) of $Co(NO_3)_2{\cdot}6H_2O$ (597 mg) and cetyl trimethyl ammonium bromide (CTAB, 20 mg) was rapidly poured into an aqueous solution (175 mL) of 2-methylimidazole (11.2 g). The mixture was continuously stirred for 5 h at 25°C. The products were centrifuged, alternately washed with deionized water as well as ethanol three times, and finally dried in a vacuum oven at 60°C.

Preparation of ZIF-67-derived N-C/Co

N-C/Co composite catalysts were prepared *via* one-step pyrolysis of ZIF-67 nanocubes. Briefly, ZIF-67 nanocubes were calcined at different temperatures for 3 h under N_2 atmosphere. The samples, such as N-C/Co-600 (600°C), N-C/Co-700 (700°C), and N-C/Co-800 (800°C), were obtained at the heating rate of 2°C min^{-1}.

Characterization

The microstructures of the samples were observed using a scanning electron microscope (SEM, Germany Zeiss Sigma 300) and a transmission electron microscope (TEM, Japan JEOL JEM 2100). The physical and chemical properties of the samples were studied *via* X-ray diffraction (XRD) patterns (Japan Rigaku Ultima III), X-ray photoelectron spectroscopy (XPS, USA Thermo Fisher Scientific K-Alpha), ultraviolet-visible (UV-Vis) diffuse reflectance spectroscopy (USA Perkin Elmer Lambda 950), photoluminescence (PL) spectroscopy (USA HORIBA FluoroMax-4), Raman spectroscopy (Thermo Scientific DXR2Xi), and Fourier transform infrared spectroscopy (FTIR, USA Nicolet 5700). N_2 adsorption-desorption and CO_2 adsorption isotherms were measured at 77 and 273 K, respectively, on a physisorption analyzer (USA Micromeritics ASAP 2020). Thermogravimetric (TG) curves were obtained on a thermal analyzer (Germany NETZSCH STA449 F5) at a heating rate of 5 K min^{-1} in flowing N_2. ^1H nuclear magnetic resonance (NMR) spectroscopy was performed on a spectrometer (Switzerland Bruker AVANCE III 500).

Photoelectrochemical measurements

Photoelectrochemical measurements were conducted in a standard three-electrode quartz cell. Ag/AgCl, Pt electrodes, and fluorine-doped-tin oxide glass covered with the samples (an area of 0.5 cm × 0.5 cm) were used as the reference, counter, and working electrodes, respectively. The transient photocurrent response was recorded on an electrochemical analyzer when the sample was irradiated with a xenon lamp (Shanghai CH Instruments CHI660E). The electrolyte was a mixed solution of CH_3CN, H_2O, and triethanolamine (TEOA) containing photosensitizer. Electrochemical impedance spectroscopy (EIS) was recorded on an electrochemical workstation (USA Princeton PARSTAT MC). The electrolyte was an aqueous solution of $K_3[Fe(CN)_6]$ (5 mmol L^{-1})/$K_4[Fe(CN)_6]$ (5 mmol L^{-1})/KCl (0.1 mol L^{-1}).

Photocatalytic CO_2 reduction

Photocatalytic CO_2 reduction was performed under visible light irradiation using a 300-W xenon lamp (λ > 420 nm) as the light source. N-C/Co composite (1 mg) and photosensitizer $[Ru(bpy)_3]Cl_2{\cdot}6H_2O$ (abbreviated as **Ru**, 8 mg) were dispersed in a mixed solution of CH_3CN (3 mL), H_2O (2 mL), and TEOA (1 mL). The quartz reactor was alternately evacuated and purged with CO_2 three times. Finally, the reactor was inflated with CO_2 for 30 min before photocatalysis. The reaction temperature was controlled at 30°C. Gaseous products were detected and analyzed *via* gas chromatography (GC, USA Agilent 7890B).

An isotopic labeling experiment was conducted to determine carbon sources of reduction products. The experimental process was similar to the aforementioned process. However, photocatalysis was performed under $^{13}CO_2$ atmosphere. Gaseous products were detected *via* GC-mass spectrometry (GC-MS). The manufacturer and model of MS was Agilent 5977B.

A cycling experiment was conducted to evaluate the stability of photocatalysts. The assistance of an external magnetic field could easily recycle N-C/Co composite catalysts owing to their magnetic properties. Initially, the photocatalytic CO_2 reduction was performed for 3 h after which the N-C/Co composite catalysts were recycled and redispersed in a fresh reaction solution for another run.

RESULTS AND DISCUSSION

ZIF-67 precursors were prepared *via* coprecipitation of metal ions (Co^{2+}) and organic ligands (2-methylimidazole) in the presence of CTAB at room temperature, as shown in Scheme 1. As shown in Fig. 1a and Fig. S1, the as-prepared ZIF-67 precursors showed a well-defined cubic morphology. The XRD pattern of the ZIF-67 nanocubes matched well with the simulated one and reflected high crystallinity (Fig. S2) [14,35]. The N_2 adsorption-desorption isotherms showed a high Brunauer-Emmett-Teller (BET) surface area of 1207.0 $m^2 g^{-1}$ (Fig. S3), indicating the porous characteristics of the ZIF-67 nanocubes.

Subsequently, N-C/Co composite catalysts were obtained *via* one-step pyrolysis of the ZIF-67 nanocubes, as illustrated in Scheme 1. The pyrolysis temperature significantly affects the structures and components of the final products [28,36]. TG analysis of the ZIF-67 nanocubes was performed to determine the pyrolysis temperature. The TG curve showed a rapid decrease in mass around 500–600°C (Fig. S4), which was caused by the decomposition of organic ligands. Therefore, three kinds of N-C/Co samples were obtained at pyrolysis temperatures of 600, 700, and 800°C, respectively.

As shown in Fig. S5, SEM images of the ZIF-67-derived samples showed cubic morphologies after pyrolysis treatment. However, TEM images showed that many small NPs appeared, indicating a collapse of the ZIF-67 framework (Fig. 1). In addition, FTIR and UV-Vis diffuse reflectance spectra of the ZIF-67-derived samples showed an absence of characteristic groups of the ZIF-67 nanocubes (Figs S6 and S7), which again supported the collapse of the ZIF-67 skeleton and the decom-

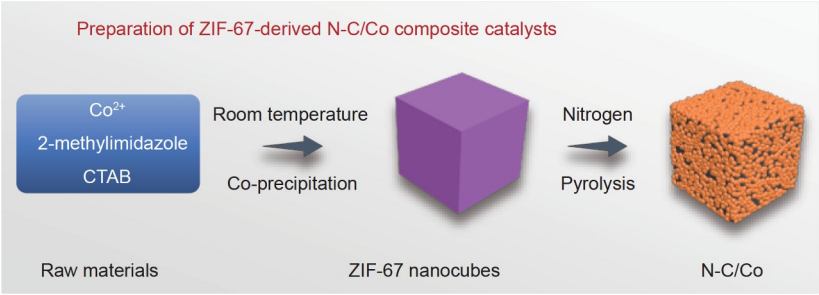

Scheme 1 Schematic shows the preparation of ZIF-67-derived N-C/Co composite catalysts.

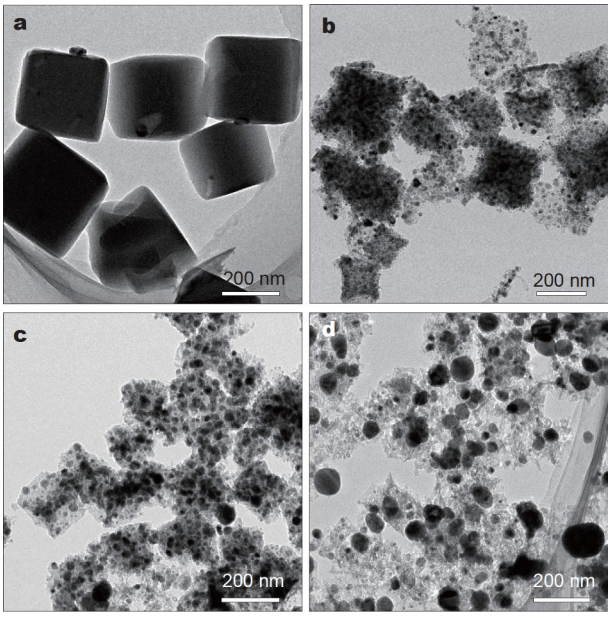

Figure 1 TEM images of ZIF-67 (a), N-C/Co-600 (b), N-C/Co-700 (c), and N-C/Co-800 (d).

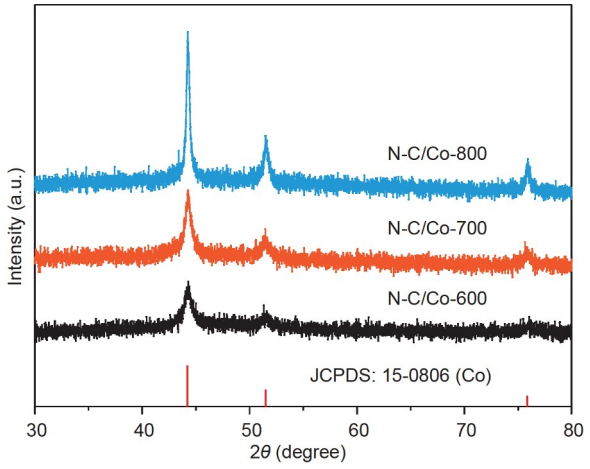

Figure 2 XRD patterns of the N-C/Co samples.

position of organic ligands. As shown in Fig. 1b–d, TEM images showed that the size of NPs increased with an increase in the pyrolysis temperature, which could be ascribed to the aggregation of Co atoms at higher temperatures. Highly magnified TEM images are shown in Fig. S5. Carbon nanotubes (CNTs) could be observed, particularly for the N-C/Co-800 sample. The catalytic effect of Co species at high temperatures can be attributed to the transformation of organic ligands into CNTs during pyrolysis [27].

The crystal phases of the ZIF-67-derived samples were determined using XRD patterns. As shown in Fig. 2, the diffraction peaks of all samples could be indexed into single-phase metallic Co (JCPDS: 15-0806). The diffraction peaks became sharper and narrower with an increase in the pyrolysis temperature. According to the Debye-Scherrer equation, the deduced average grain size of Co NPs was smaller for the N-C/Co-600 sample than those of other samples. The results of XRD patterns were consistent with the TEM observation. Raman spectra were performed to reveal the presence of carbon matrix. As shown in Fig. S8, two prominent peaks at 1338 and 1589 cm^{-1} were assigned to D-band and G-band, respectively, which were characteristic Raman peaks of defective carbon and graphitic carbon [37,38]. Considering the incorporation of N elements into 2-methylimidazole, the N-doped C matrix was obtained after pyrolysis treatment [39,40]. From the aforementioned characterization results, it could be concluded that Co NPs were distributed on the N-doped C matrix after the pyrolysis of ZIF-67 nanocubes.

To reveal detailed information about the as-prepared composite catalysts, high-resolution TEM (HRTEM) was performed. The N-C/Co-600 sample was selected for the study. As shown in Fig. 3a, Co NPs can be distinguished from the N-C matrix owing to the different contrast under TEM observation. Co NPs were well encapsulated in N-C layers and separated from each other owing to the outside N-C coating. Such a unique combination was ascribed to the highly ordered arrangement of metal ions and organic ligands in the ZIF-67 framework, which contributed to the good dispersion of NPs. The lattice fringes of Co NPs were well defined. The interplanar distance was measured to be ~0.208 nm, corresponding to the (111) crystal planes of Co. Selected area electron diffraction (SAED) patterns showed the polycrystalline nature of the N-C/Co-600 sample, as shown in Fig. 3b. The elemental mappings of the N-C/Co-600 sample showed homogeneous distributions of C, N, and Co elements, indicating a good combination of the N-C matrix and Co NPs.

The components of the N-C/Co samples were analyzed *via* XPS. As shown in Fig. S9, the survey spectra showed the presence of C, N, and Co species for all samples. It is widely recognized that the increased catalytic sites are beneficial to CO_2 activation [4,38,41]. Co contents that were determined from XPS analysis decreased with an increase in the pyrolysis temperature (Fig. S9), which was caused by the aggregation of Co atoms at high temperatures. The aggregation of Co atoms also increased

the grain size of Co NPs, which were revealed by XRD patterns and TEM images. High-Co content and a small grain size could increase catalytic sites and then promote photocatalytic CO_2 reduction.

High-resolution XPS (HRXPS) spectrum of Co $2p_{3/2}$ of the N-C/Co-600 sample is shown in Fig. 4a. The Co $2p_{3/2}$ peak was deconvoluted into Co^0 (777.5 eV), Co^{3+} (779.2 eV), and Co^{2+} (781.6 eV), along with a satellite peak (785.8 eV) [30,42], indicating the presence of CoO_x oxides on the surface of Co NPs. However, no oxide was observed in the XRD patterns (Fig. 2a), which was probably due to the amorphous nature of surface oxides or the resolution difference between XRD and XPS [31]. HRXPS spectra of the Co $2p_{3/2}$ of the N-C/Co-700 and N-C/Co-800 samples also showed similar chemical configurations. However, the peak intensity of Co^0 gradually decreased as the pyrolysis temperature increased. The contents of metallic Co^0 and oxidized Co^{2+} and Co^{3+} are shown in Table S1. The different contents of metallic Co^0 at different pyrolysis temperatures were

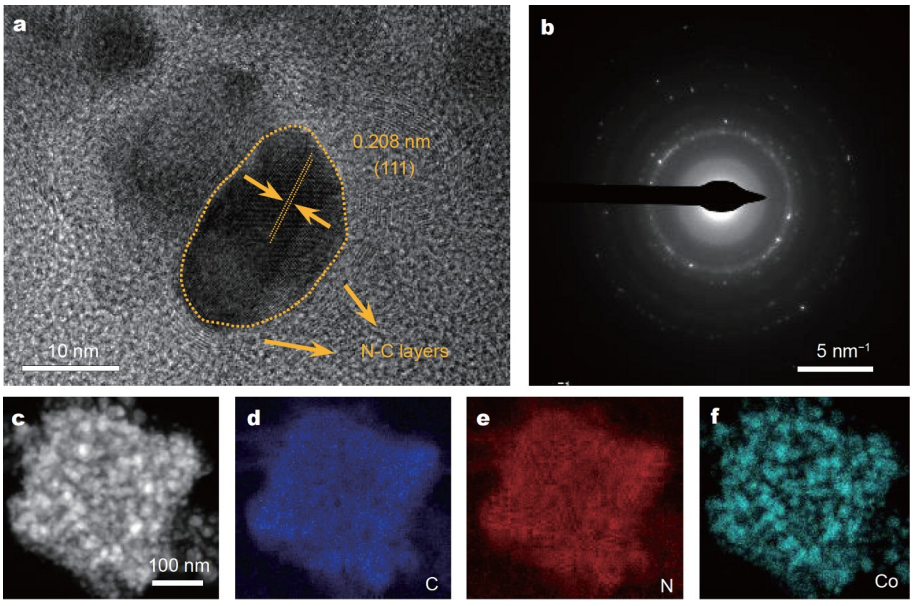

Figure 3 (a) HRTEM image, (b) SAED pattern, and (c–f) elemental mappings of the N-C/Co-600 sample.

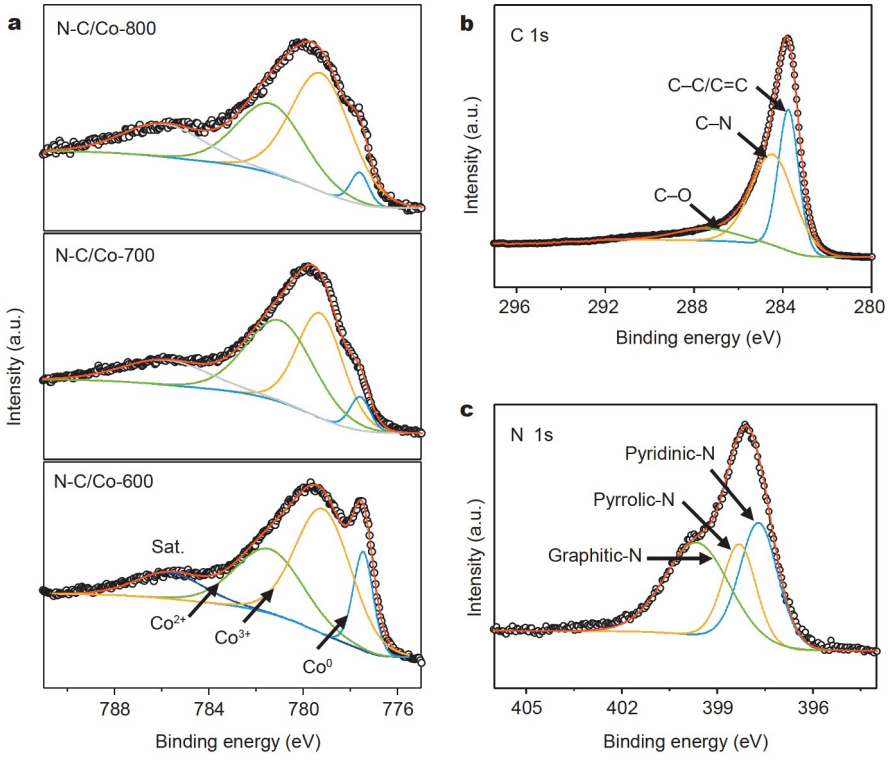

Figure 4 HRXPS spectra of (a) Co $2p_{3/2}$ of the N-C/Co samples, (b) C 1s and (c) N 1s of the N-C/Co-600 sample.

associated with the grain size of Co NPs. The grain size of Co NPs was larger for the N-C/Co sample obtained at a higher pyrolysis temperature, which had been confirmed by XRD patterns and TEM images. As a result, it was difficult for the outside N-C layers to entirely wrap the large Co NPs, which further increased the exposure of metallic Co to air. Therefore, surface oxidation was accelerated, accompanied by the coverage of inside Co cores.

The HRXPS spectrum of C 1s was composed of C–C/C=C, C–N, and C–O [34, 37, 40], as shown in Fig 4b. The existence of the C–N bond manifested the doping of nitrogen in the carbon matrix. The surface-N contents in the N-C/Co samples were first determined from XPS spectra. As shown in Fig. S9, the overall N content decreased as the pyrolysis temperature increased. The N doping could facilitate the CO_2 uptake of carbon [43]. The N-C/Co-600 and N-C/Co-700 samples with higher N contents exhibited greater CO_2 uptake abilities than the N-C/Co-800 sample (Fig. S10). In addition, as shown in Fig. 4c, the HRXPS spectrum of N 1s was deconvoluted into pyridinic-N, pyrrolic-N, and graphitic-N [36,42]. Previous studies [32,33] have reported that nitrogen doping could improve the photochemical performances of carbon materials by influencing their electronic and chemical properties [44]. Thus, the outside N-C layers are important for efficient photocatalytic CO_2 reduction. They could act as bridges to transfer electrons from photosensitizer to inside Co cores. Furthermore, the contents of N species in the N-C/Co samples were determined from the HRXPS spectra of N 1s. As shown in Fig. S11 and Table S2, when the pyrolysis temperature increased from 600 to 800°C, the graphitic-N content increased, whereas the pyridinic-N and pyrrolic-N contents decreased. The higher pyridinic-N and pyrrolic-N contents in the N-C/Co-600 samples could contribute to improved electron transfer efficiency [45].

Photocatalytic CO_2 reduction was performed to evaluate the catalytic activities of the N-C/Co samples. The photosensitizer **Ru** was used to provide reductive electrons. Reduction products and gas yields were recorded *via* GC. Gas yields for different N-C/Co samples were shown in Fig. 5a. The main reduction products were CO and hydrogen (H_2). An almost equal amount of H_2 was produced, along with CO. Co has been demonstrated as a wonderful H_2 evolution catalyst [13,46,47]. Therefore, the H_2 evolution reaction could proceed, along with the photocatalytic CO_2 reduction reaction. As a result, syngas with a CO/H_2 ratio close to 1:1 was obtained from photocatalytic CO_2 reduction. In

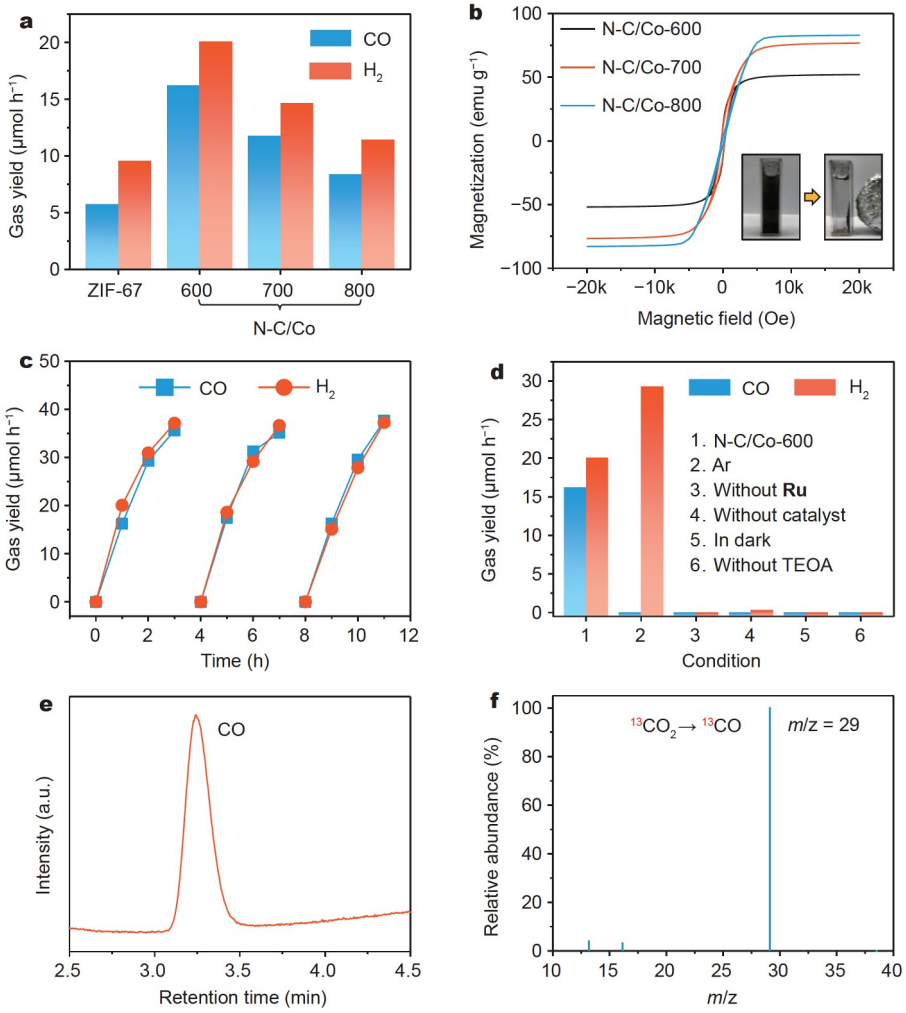

Figure 5 (a) Gas yields for different samples. (b) Magnetization curves of the N-C/Co samples. (c) Gas yield for the N-C/Co-600 sample in a cycling experiment. (d) Gas yields for the N-C/Co-600 sample under different conditions. (e) GC spectrum and (f) MS spectrum of the reduction products in $^{13}CO_2$ isotopic labeling experiment.

addition, ^{1}H NMR spectra were performed to detect liquid products. As shown in Fig. S12, no liquid products, such as HCHO, CH_3OH, and HCOOH, could be detected. In general, CO_2 reduction involved multistep electron transfer steps and various reduction products could be generated. The final reduction products are typically dependent on kinetic and thermodynamic factors [48]. For example, it is thermodynamically favorable for the CH_4 formation owing to the lower potential. However, the formation of CH_4 requires eight electrons, whereas only two electrons are required to generate CO and H_2 [8]. As a result, the main products from the photocatalytic CO_2 reduction consisted of CO and H_2 in this work.

In addition, the influence of catalyst content on the catalytic activity was assessed. As shown in Fig. S13, as the catalyst content increased from 1 to 4 mg, gas yields increased from 16.20 (CO)/20.06 (H_2) to 26.62 (CO)/35.51 (H_2) μmol h^{-1}. However, the gas generation rates decreased from 1.62×10^4 (CO)/2.01×10^4 (H_2) to 6655 (CO)/8878 (H_2) μmol g^{-1} h^{-1}, which could be attributed to the restricted mass-transport or the light-shielding effect due to the excessive catalysts [14].

Fig. 5a showed that the catalytic activities of all N-C/Co samples were superior to that of pristine ZIF-67 nanocubes. The low gas yields for the ZIF-67 nanocubes could be ascribed to the sluggish charge transfer owing to their low electric conductivity [32,33]. In addition, gas yields decreased as the pyrolysis temperature increased. Particularly, the N-C/Co-600 sample afforded the highest gas yields. CO and H_2 yields were as high as 16.20 and 20.06 μmol at the first hour, with gas generation rates of 1.62×10^4 and 2.01×10^4 μmol g^{-1} h^{-1}, respectively. Due to the outstanding catalytic activity of the N-C/Co-600 sample, gas generation was visible to the naked eye during photocatalytic CO_2 reduction. As shown in Movie S1, a large number of bubbles were produced once the photocatalytic reactor was irradiated using a xenon lamp (λ > 420 nm). The comparison of catalytic activities of photocatalytic CO_2 reduction between the N-C/Co-600 composite catalyst and other state-of-the-art photocatalysts is listed in Table S3. The catalytic activity of the N-C/Co-600 composite catalyst reported in this work was comparable or even superior to many other catalysts.

In addition, Co NPs made the composite catalysts magnetic. As shown in Fig. 5b, the magnetization curves showed a hysteresis loop, indicating the magnetic property of the samples. The saturation magnetization of the N-C/Co-600, N-C/Co-700, and N-C/Co-800 samples was 51.9, 76.7, and 82.8 emu g^{-1}, respectively. The magnetic property allowed the rapid recycling of catalysts from the solution (inset of Fig. 5b). With this advantage, the cycling stability of the N-C/Co-600 sample was performed every 3 h with the help of magnetic separation. During three continuous runs, gas yields were steady with a small fluctuation (Fig. 5c), demonstrating the high stability of the N-C/Co-600 sample. The sample after the photocatalytic reaction was collected for XRD and SEM analysis to reveal the change in structure. As shown in Fig. S14, the crystal phase and morphology of the N-C/Co-600 sample remained almost unchanged after the reaction, confirming the high stability of the sample.

Photocatalytic factors were also studied by performing photocatalytic CO_2 reduction under various reaction conditions. In the normal condition (column 1 of Fig. 5d), almost equal amounts of CO and H_2 were produced. When the photocatalytic CO_2 reduction was performed under Ar atmosphere (column 2 of Fig. 5d), H_2 was the dominant reduction product. On the one hand, the H_2 evolution reaction proceeded without CO_2 molecules, indicating the strong H_2 evolution ability of the N-C/Co-600 sample. On the other hand, the absence of CO suggested that CO was produced from CO_2 rather than other potential carbon sources. The isotopic labeling experiment was conducted to trace the ^{13}C signal of $^{13}CO_2$. GC-MS analysis is shown in Fig. 5e, f. A predominant signal at m/z = 29 was assigned to ^{13}CO, which again supported that CO came from CO_2 molecules. The presence of **Ru** greatly influenced the photocatalytic CO_2 reduction. In the absence of **Ru**, CO_2 molecules could not be reduced (column 3 of Fig. 5d). The photosensitizer **Ru** played two roles in photocatalytic processes, including harvesting visible light and producing reductive electrons. In the absence of samples (column 4 of Fig. 5d), almost no products could be detected, suggesting the role of the N-C/Co samples in accepting electrons from the photosensitizer **Ru**. In addition, because CO_2 reduction was a photocatalytic process, it was rational that there was no gas generating in the dark (column 5 of Fig. 5d). Furthermore, the sacrificial agent TEOA was indispensable for efficient photocatalytic reduction of CO_2 (column 6 of Fig. 5d).

To reveal the origin of the difference in catalytic activities of different N-C/Co samples, a series of photoelectrochemical measurements were performed. Under visible light irradiation, the electron-hole pairs were separated, and electrons were transferred from the photosensitizer **Ru** to the samples. The charge separation and transfer were evaluated using EIS plots, transient photocurrent response, and PL spectra. As shown in Fig. 6a, the radii of semicircles of all N-C/Co samples were much smaller than that of pristine ZIF-67 nanocubes, indicating that the charge transfer resistance was considerably diminished after pyrolysis treatment. The low electric conductivity of ZIF-67 accounted for this difference, which made the charge transfer sluggish, resulting in inefficient CO_2 reduction. Owing to the high contents of metallic Co^0, pyridinic-N, and pyrrolic-N, the N-C/Co-600 sample possessed the smallest semicircle among all samples. The photocurrent response supported the results of EIS plots. As shown in Fig. 6b, the curve of the photocurrent density of the ZIF-67 nanocubes was distinct from that of the N-C/Co samples, suggesting a great difference in intrinsic photoelectronic properties. The N-C/Co-600 sample had the highest current density, followed by N-C/Co-700, N-C/Co-800, and ZIF-67. Because photocurrent was produced by the directional movement of electrons, the strong photocurrent response manifested that electron transfer was significantly accelerated for the N-C/Co-600 sample. The rapid electron transfer could inhibit electron recombination with holes, as verified by the PL spectra (Fig. 6c). PL quenching was observed after introducing samples into a solution of the photosensitizer **Ru**. Because PL was caused by the recombination of electrons and holes [13], the lowest PL intensity of the N-C/Co-600 sample reflected the most efficient electron-hole separation between the photosensitizer **Ru** and catalysts [16]. Overall, the introduction of catalysts greatly suppressed the recombination of charged carriers over the photosensitizer **Ru** by accelerating electron migration to the N-C/Co composites catalysts. Because of the N-C layers and metallic Co^0, the N-C/Co-600 sample became considerably more accessible to the photoexcited electrons, promoting both CO_2 reduction and H_2 evolution reactions to generate CO and H_2.

BET surface areas and CO_2 uptake abilities of the N-C/Co samples were measured. BET surface areas of the N-C/Co-600,

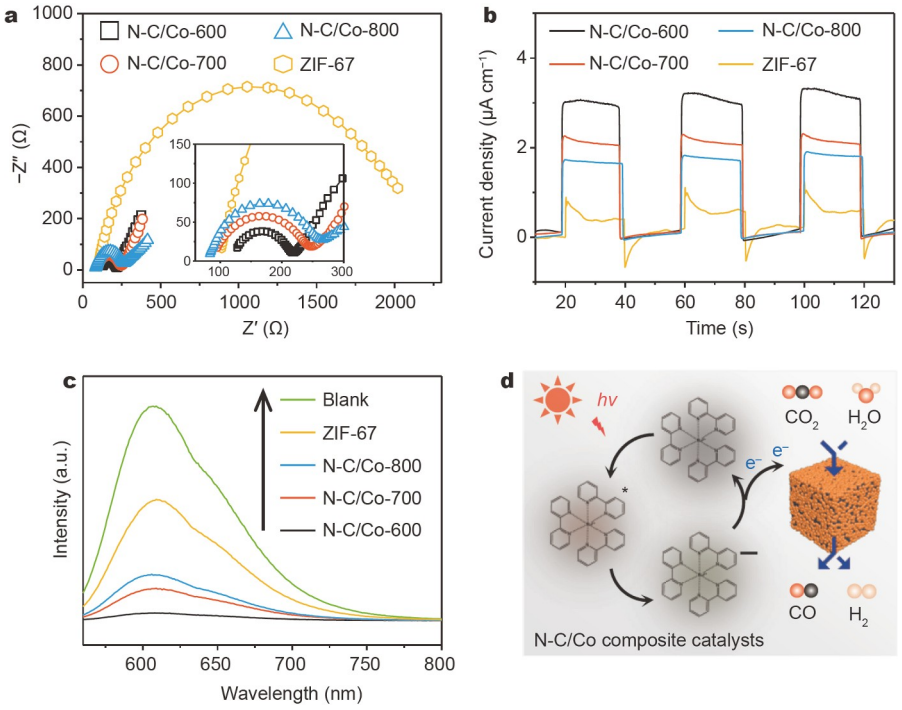

Figure 6 (a) EIS plots. (b) Photocurrent response. (c) PL spectra. (d) Schematic of the proposed photocatalytic mechanism.

N-C/Co-700, and N-C/Co-800 samples were determined to be 166.7, 226.5, and 197.6 $cm^2 g^{-1}$, respectively, from the N_2 adsorption-desorption isotherms (Fig. S15). Although the N-C/Co-600 sample had the smallest BET surface area among the three samples, it showed the best catalytic performance. By contrast, the pristine ZIF-67 with an ultrahigh BET surface area of 1207.0 $cm^2 g^{-1}$ (Fig. S3) afforded the lowest catalytic activity (Fig. 5a). In addition, the maximum CO_2 adsorption amounts of the N-C/Co-600, N-C/Co-700, and N-C/Co-800 samples were determined to be 27.1, 27.5, and 19.1 $cm^3 g^{-1}$, respectively, from CO_2 adsorption isotherms (Fig. S10). The N-C/Co-600 and N-C/Co-700 samples with large CO_2 adsorption capacities showed high photocatalytic activities than the N-C/Co-800 sample, indicating the importance of CO_2 adsorption for efficient CO_2 reduction. However, the N-C/Co-700 sample with the largest CO_2 adsorption did not exhibit the highest gas yields. These results suggested that BET surface areas and CO_2 uptake abilities were favorable for CO_2 photoreduction but not decisive factors in this work.

The comparison of sample information and catalytic activities among the N-C/Co-600, N-C/Co-700, and N-C/Co-800 samples is listed in Table S4. The N-C/Co-600 sample with small grain size and high metallic Co^0 content significantly improved charge separation and electron transfer, resulting in the most efficient CO_2 reduction. Based on the above discussion, the photocatalytic mechanism of CO_2 reduction with N-C/Co composite catalysts was proposed, as illustrated in Fig. 6d. The excitation of the photosensitizer $Ru(bpy)_3^{2+}$ under visible light produced an excited state $Ru(bpy)_3^{2+}$*, which was further quenched by TEOA to produce a reduced species $Ru(bpy)_3^{+}$. The excellent electrical conductivity of the N-C/Co-600 sample made electron transfer favorable from reduced species $Ru(bpy)_3^{+}$ to the composite catalyst. The adsorbed CO_2 molecules on the N-C/Co-600 sample were subsequently reduced by electrons to generate CO. Since Co was a good H_2 evolution catalyst, the H_2O molecules were also reduced by electrons to generate H_2. Overall, the N-C/Co-600 composite catalyst played two critical roles in efficient photocatalytic CO_2 reduction, including providing catalytic sites for CO_2 adsorption and activation and serving as electron acceptors for accelerating electron transfer.

CONCLUSIONS

In conclusion, we demonstrated that the N-C/Co composite catalysts are built by encapsulating Co NPs in N-C layers with ZIF-67 nanocubes as precursors. The outside N-C layers avoided the agglomeration of Co NPs and increased electric conductivity, whereas the inside Co NPs acted as catalytic sites and electron acceptors for photocatalytic CO_2 reduction. The N-C/Co samples obtained at low pyrolysis temperatures showed better catalytic activities. As discussed above, the synergistic effect of different factors could be responsible for the improved photocatalytic CO_2 reduction. We ascribed the improved catalytic activity to the following aspects: (1) as revealed by XRD patterns, TEM images, and XPS spectra, the aggregation of Co NPs at high temperatures resulted in large grains and low Co content, which significantly decreased catalytic sites; (2) the surface oxidation of Co NPs was effectively inhibited by controlling the pyrolysis temperature and grain size. The samples that showed better photocatalytic performance contained higher contents of metallic Co^0, pyridinic-N, and pyrrolic-N. These components contributed to the accelerated charge separation and transfer, finally leading to high CO and H_2 yields. In this work, we have developed a facile method for controlling structures and components of ZIF-67-derived N-C/Co composite catalysts and

modulating the photocatalytic activity of CO_2 reduction.

Received 27 April 2021; accepted 13 July 2021; published online 6 September 2021

1 Li X, Yu J, Jaroniec M, *et al.* Cocatalysts for selective photoreduction of CO_2 into solar fuels. Chem Rev, 2019, 119: 3962–4179
2 Zhong W, Sa R, Li L, *et al.* A covalent organic framework bearing single Ni sites as a synergistic photocatalyst for selective photoreduction of CO_2 to CO. J Am Chem Soc, 2019, 141: 7615–7621
3 Chen K, Wang X, Li Q, *et al.* Spatial distribution of $ZnIn_2S_4$ nanosheets on g-C_3N_4 microtubes promotes photocatalytic CO_2 reduction. Chem Eng J, 2021, 418: 129476
4 Yi L, Zhao W, Huang Y, *et al.* Tungsten bronze $Cs_{0.33}WO_3$ nanorods modified by molybdenum for improved photocatalytic CO_2 reduction directly from air. Sci China Mater, 2020, 63: 2206–2214
5 Han C, Li J, Ma Z, *et al.* Black phosphorus quantum dot/g-C_3N_4 composites for enhanced CO_2 photoreduction to CO. Sci China Mater, 2018, 61: 1159–1166
6 He Y, Chen X, Huang C, *et al.* Encapsulation of Co single sites in covalent triazine frameworks for photocatalytic production of syngas. Chin J Catal, 2021, 42: 123–130
7 Chen L, Wang X, Chen Y, *et al.* Recycling heavy metals from wastewater for photocatalytic CO_2 reduction. Chem Eng J, 2020, 402: 125922
8 Chang X, Wang T, Gong J. CO_2 photo-reduction: Insights into CO_2 activation and reaction on surfaces of photocatalysts. Energy Environ Sci, 2016, 9: 2177–2196
9 Zhang Y, Xia B, Ran J, *et al.* Atomic-level reactive sites for semiconductor-based photocatalytic CO_2 reduction. Adv Energy Mater, 2020, 10: 1903879
10 Wang X, Chen J, Li Q, *et al.* Light-driven syngas production over defective $ZnIn_2S_4$ nanosheets. Chem Eur J, 2021, 27: 3786–3792
11 Zhuang G, Chen Y, Zhuang Z, *et al.* Oxygen vacancies in metal oxides: Recent progress towards advanced catalyst design. Sci China Mater, 2020, 63: 2089–2118
12 Xu F, Meng K, Cheng B, *et al.* Unique S-scheme heterojunctions in self-assembled TiO_2/$CsPbBr_3$ hybrids for CO_2 photoreduction. Nat Commun, 2020, 11: 4613
13 Han B, Ou X, Deng Z, *et al.* Nickel metal-organic framework monolayers for photoreduction of diluted CO_2: Metal-node-dependent activity and selectivity. Angew Chem Int Ed, 2018, 57: 16811–16815
14 Chen W, Han B, Tian C, *et al.* MOFs-derived ultrathin holey Co_3O_4 nanosheets for enhanced visible light CO_2 reduction. Appl Catal B-Environ, 2019, 244: 996–1003
15 Wang D, Huang R, Liu W, *et al.* Fe-based MOFs for photocatalytic CO_2 reduction: Role of coordination unsaturated sites and dual excitation pathways. ACS Catal, 2014, 4: 4254–4260
16 Tan L, Xu SM, Wang Z, *et al.* Highly selective photoreduction of CO_2 with suppressing H_2 evolution over monolayer layered double hydroxide under irradiation above 600 nm. Angew Chem Int Ed, 2019, 58: 11860–11867
17 Wang XK, Liu J, Zhang L, *et al.* Monometallic catalytic models hosted in stable metal-organic frameworks for tunable CO_2 photoreduction. ACS Catal, 2019, 9: 1726–1732
18 Gao C, Chen S, Wang Y, *et al.* Heterogeneous single-atom catalyst for visible-light-driven high-turnover CO_2 reduction: The role of electron transfer. Adv Mater, 2018, 30: 1704624
19 Sun X, Habibul N, Du H. $Co_{0.85}Se$ magnetic nanoparticles supported on carbon nanotubes as catalyst for hydrogen evolution reaction. Chin J Catal, 2021, 42: 235–243
20 Bie C, Yu H, Cheng B, *et al.* Design, fabrication, and mechanism of nitrogen-doped graphene-based photocatalyst. Adv Mater, 2021, 33: 2003521
21 Chen W, Han B, Xie Y, *et al.* Ultrathin Co-Co LDHs nanosheets assembled vertically on MXene: 3D nanoarrays for boosted visible-light-driven CO_2 reduction. Chem Eng J, 2020, 391: 123519
22 Trickett CA, Helal A, Al-Maythalony BA, *et al.* The chemistry of metal-organic frameworks for CO_2 capture, regeneration and conversion. Nat Rev Mater, 2017, 2: 17045
23 Xiao JD, Jiang HL. Metal-organic frameworks for photocatalysis and photothermal catalysis. Acc Chem Res, 2019, 52: 356–366
24 Zhan W, Sun L, Han X. Recent progress on engineering highly efficient porous semiconductor photocatalysts derived from metal-organic frameworks. Nano-Micro Lett, 2019, 11: 1
25 Wu J, Wang S, Lei Z, *et al.* Pomegranate-like C_{60}@cobalt/nitrogen-codoped porous carbon for high-performance oxygen reduction reaction and lithium-sulfur battery. Nano Res, 2020, doi: 10.1007/s12274-020-3260-4
26 Wang L, Wan J, Zhao Y, *et al.* Hollow multi-shelled structures of Co_3O_4 dodecahedron with unique crystal orientation for enhanced photocatalytic CO_2 reduction. J Am Chem Soc, 2019, 141: 2238–2241
27 Chen Z, Wu R, Liu Y, *et al.* Ultrafine Co nanoparticles encapsulated in carbon-nanotubes-grafted graphene sheets as advanced electrocatalysts for the hydrogen evolution reaction. Adv Mater, 2018, 30: 1802011
28 Xu Y, Tu W, Zhang B, *et al.* Nickel nanoparticles encapsulated in few-layer nitrogen-doped graphene derived from metal-organic frameworks as efficient bifunctional electrocatalysts for overall water splitting. Adv Mater, 2017, 29: 1605957
29 Zhang H, Wang T, Wang J, *et al.* Surface-plasmon-enhanced photodriven CO_2 reduction catalyzed by metal-organic-framework-derived iron nanoparticles encapsulated by ultrathin carbon layers. Adv Mater, 2016, 28: 3703–3710
30 Zhang M, Dai Q, Zheng H, *et al.* Novel MOF-derived Co@N-C bifunctional catalysts for highly efficient Zn-air batteries and water splitting. Adv Mater, 2018, 30: 1705431
31 Tian H, Zhang C, Su P, *et al.* Metal-organic-framework-derived formation of Co-N-doped carbon materials for efficient oxygen reduction reaction. J Energy Chem, 2020, 40: 137–143
32 Zhao K, Zhao S, Gao C, *et al.* Metallic cobalt-carbon composite as recyclable and robust magnetic photocatalyst for efficient CO_2 reduction. Small, 2018, 14: 1800762
33 Lin X, Wang S, Tu W, *et al.* Magnetic hollow spheres assembled from graphene-encapsulated nickel nanoparticles for efficient photocatalytic CO_2 reduction. ACS Appl Energy Mater, 2019, 2: 7670–7678
34 Liu H, Chen Z, Zhou L, *et al.* Rooting bismuth oxide nanosheets into porous carbon nanoboxes as a sulfur immobilizer for lithium–sulfur batteries. J Mater Chem A, 2019, 7: 7074–7081
35 Qin J, Wang S, Wang X. Visible-light reduction CO_2 with dodecahedral zeolitic imidazolate framework ZIF-67 as an efficient co-catalyst. Appl Catal B-Environ, 2017, 209: 476–482
36 Wang L, Wang Z, Xie L, *et al.* ZIF-67-derived N-doped Co/C nanocubes as high-performance anode materials for lithium-ion batteries. ACS Appl Mater Interfaces, 2019, 11: 16619–16628
37 Chen FF, Zhu YJ, Chen F, *et al.* Fire alarm wallpaper based on fire-resistant hydroxyapatite nanowire inorganic paper and graphene oxide thermosensitive sensor. ACS Nano, 2018, 12: 3159–3171
38 Xia Y, Cheng B, Fan J, *et al.* Near-infrared absorbing 2D/3D $ZnIn_2S_4$/N-doped graphene photocatalyst for highly efficient CO_2 capture and photocatalytic reduction. Sci China Mater, 2020, 63: 552–565
39 Du Z, Yu P, Wang L, *et al.* Cubic imidazolate frameworks-derived CoFe alloy nanoparticles-embedded N-doped graphitic carbon for discharging reaction of Zn-air battery. Sci China Mater, 2020, 63: 327–338
40 Peng W, Yang X, Mao L, *et al.* ZIF-67-derived Co nanoparticles anchored in N doped hollow carbon nanofibers as bifunctional oxygen electrocatalysts. Chem Eng J, 2021, 407: 127157
41 Li Y, Li X, Zhang H, *et al.* Design and application of active sites in g-C_3N_4-based photocatalysts. J Mater Sci Tech, 2020, 56: 69–88
42 Amiinu IS, Liu X, Pu Z, *et al.* From 3D ZIF nanocrystals to Co-N_x/C nanorod array electrocatalysts for ORR, OER, and Zn-air batteries. Adv Funct Mater, 2018, 28: 1704638
43 Xing W, Liu C, Zhou Z, *et al.* Superior CO_2 uptake of N-doped activated carbon through hydrogen-bonding interaction. Energy Environ Sci, 2012, 5: 7323–7327
44 Wang S, Guan BY, Lou XWD. Rationally designed hierarchical N-doped carbon@$NiCo_2O_4$ double-shelled nanoboxes for enhanced visible light CO_2 reduction. Energy Environ Sci, 2018, 11: 306–310

45 Xie X, Su D, Zhang J, *et al.* A comparative investigation on the effects of nitrogen-doping into graphene on enhancing the electrochemical performance of SnO_2/graphene for sodium-ion batteries. Nanoscale, 2015, 7: 3164–3172
46 Lee JS, Won DI, Jung WJ, *et al.* Widely controllable syngas production by a dye-sensitized TiO_2 hybrid system with Re^{I} and Co^{III} catalysts under visible-light irradiation. Angew Chem Int Ed, 2017, 56: 976–980
47 Liu M, Mu YF, Yao S, *et al.* Photosensitizing single-site metal-organic framework enabling visible-light-driven CO_2 reduction for syngas production. Appl Catal B-Environ, 2019, 245: 496–501
48 Li X, Sun Y, Xu J, *et al.* Selective visible-light-driven photocatalytic CO_2 reduction to CH_4 mediated by atomically thin $CuIn_5S_8$ layers. Nat Energy, 2019, 4: 690–699

Acknowledgements This work was financially supported by the National Key Research and Development Program of China (2020YFA0710303) and the National Natural Science Foundation of China (51972061, U1905215 and 52072076).

Author contributions Chen FF and Chen J conducted the experiments; Chen FF wrote the manuscript; Feng YN contributed to data analysis; Li L and Yu Y conceived the idea of this work and revised the manuscript. All authors contributed to the general discussion.

Conflict of interest The authors declare that they have no conflict of interest.

Supplementary information Supporting data are available in the online version of the paper.

Fei-Fei Chen received his BS degree in 2014 from Xiamen University and his PhD degree in 2019 from Shanghai Institute of Ceramics, Chinese Academy of Sciences. Currently, he is a lecturer at Fuzhou University. His research interests include photocatalytic CO_2 reduction, water purification, ecological materials, low-dimensional inorganic nanostructures, and metal-organic framework-derived catalysts.

Jianfeng Chen received his BS degree in 2018 from Fujian Agriculture and Forestry University. Currently, he is an MS candidate under the supervision of Prof. Yan Yu at Fuzhou University. His research interests include photocatalytic CO_2 reduction, metal-organic frameworks, and metal-organic framework-derived catalysts.

Lingyun Li received his BS degree in 2007 from Hefei University of Technology and his PhD degree in 2012 from Fujian Institute of Research on the Structure of Matter, Chinese Academy of Sciences. Currently, he is an associate professor at Fuzhou University. His research interests include optical materials, laser crystals, metal-organic frameworks, and environmental remediation.

Yan Yu received her BS, MS, and PhD degrees from Fuzhou University. She was a postdoctoral fellow in 2010–2013 at Fujian Institute of Research on the Structure of Matter, Chinese Academy of Sciences. Currently, she is a professor at Fuzhou University. Her research interests include environmental remediation, water purification, ecological materials, photocatalytic CO_2 reduction and H_2 production.

调控ZIF-67衍生N-C/Co复合催化剂中的金属性Co^0实现高效光催化CO_2还原

陈飞飞[†], 陈建丰[†], 冯亚南, 李凌云[*], 于岩[*]

摘要 本文报道了由ZIF-67衍生而来的N掺杂C层包裹Co纳米颗粒(N-C/Co)复合催化剂及其高效光催化CO_2还原性能. 研究发现热解温度对N-C/Co复合催化剂的晶粒尺寸和金属性Co^0含量的调控具有关键作用, 并在此基础上优化了催化剂的光催化活性. 在较低热解温度(600°C)下获得的Co纳米颗粒尺寸较小, 能够被N-C层良好保护, 从而有效抑制表面氧化, 使得N-C/Co-600样品中具有更高含量的金属性Co^0. 相反, N-C/Co-700和N-C/Co-800样品中的表面氧化物CoO_x覆盖了内部Co核, 不利于电荷分离和迁移. 因此, N-C/Co-600样品表现出最佳的光催化活性. CO和H_2的产率分别高达1.62 × 10^4和2.01 × 10^4 μmol g^{-1} h^{-1}. 另外, Co纳米颗粒使得复合催化剂具有磁性, 能够在外加磁场辅助下, 快速、简易地分离回收. 本工作有望为MOF衍生碳/金属复合催化剂的设计提供参考依据.

